Extremum-Seeking-Based Fluctuation Mitigation and Azimuthal Velocity Profile Regulation by $E \times B$ Actuation in HELCAT

Zeki Okan Ilhan, Qiaoqiao Wang, Jason Barry, David Huxley-Cohen, Hexiang Wang, Eugenio Schuster, Shuangwei Xie, Mark Gilmore, and Andrew Ware

***Abstract*— Turbulence and turbulence-driven transport are ubiquitous in magnetically confined plasmas, where there is an intimate relationship between turbulence, transport, destabilizing mechanisms, such as gradients and currents, and stabilizing mechanisms like shear. Active control of fluctuations is investigated in this paper via manipulation of flow profiles in a magnetized laboratory plasma device helicon–cathode (HELCAT). Fluctuations are monitored by electrostatic probes, and $E \times B$ flow profiles are controlled via bias ring electrodes. First, a nonmodel-based extremum-seeking optimal control algorithm is implemented in HELCAT to seek the bias ring voltages that minimize a cost function related to the fluctuation amplitude. The experimental results in HELCAT show that the proposed controller is able to not only suppress the fluctuations but also to regulate their average amplitude around a predefined desired level. It is anticipated that this controller can become a valuable tool for physics-oriented studies designed to elucidate the relationship between the shape of the azimuthal flow profile and the amplitude of the fluctuations once the capability of measuring the flow profile in real time becomes available in HELCAT. Second, with the assistance of a HELCAT-tailored transport code capable of predicting the evolution of the azimuthal flow at several radial points within the plasma, the potential of an extremum-seeking controller for directly regulating the azimuthal flow profile around a prescribed target profile is illustrated numerically.**

***Index Terms*— Extremum seeking, plasma transport control.**

I. Introduction

VARIOUS magnetic confinement devices have been designed so far to carry out a wide range of plasma experiments in laboratory environments. Plasma processes usually span a wide range of parameters covering several orders of magnitude in density, temperature, and magnetic field strength. However, laboratory experiments are in general limited by the range of parameter space the plasma generation mechanism can access. Considering these limitations, the helicon–cathode (HELCAT) device (Fig. 1) has been designed and built to access a wide range of parameters in a modest scale laboratory device [1]. One of the objectives of HELCAT is to establish the feasibility of using advanced control algorithms to control cross-field turbulence-driven particle transport through appropriate manipulation of radial plasma flow profiles [2].

Fig. 1. HELCAT device at University of New Mexico.

Though many of the detailed physics of the interrelationship between turbulence, transport drive mechanisms, and flow remain unclear, there is a clear experimental evidence in both fusion and laboratory plasmas that transport and/or turbulence can be suppressed or reduced via shaping of plasma flow profiles (flow shear) [3], [4]. Several theories were proposed to explain this phenomenon. Currently, the most accepted cause for transport mitigation is the reduction and/or stabilization of turbulence by sheared $E \times B$ flow profiles [4]. In the HELCAT device, the $E \times B$ flow (or, azimuthal flow, V_θ) is generated by the azimuthal force created by the interaction of the axial magnetic field (B) due to the magnets surrounding the plasma column and the radial electric field (E_r) imposed by the set of biased concentric ring electrodes that terminate the plasma column.

The ultimate goal of this paper is to establish the feasibility of using advanced active control algorithms to control cross-field turbulence-driven particle transport through appropriate manipulation of radial plasma flow profiles. This paper reports progress toward this goal. First, an open-loop

Manuscript received August 8, 2013; accepted December 11, 2013. Date of publication February 11, 2014; date of current version March 6, 2014. This work was supported in part by the National Science Foundation under Grant PHY-0903803 and Grant PHY-0913663, and in part by the U.S. Department of Energy under Grant DE-FG02-09ER55022 and Grant DE-SC0001039.

Z. O. Ilhan, Q. Wang, J. Barry, D. Huxley-Cohen, H. Wang, and E. Schuster are with the Department of Mechanical Engineering and Mechanics, Lehigh University, Bethlehem, PA 18015 USA (e-mail: zoi210@lehigh.edu; schuster@lehigh.edu).

S. Xie and M. Gilmore are with the Department of Electrical and Computer Engineering, University of New Mexico, Albuquerque, NM 87131 USA (e-mail: gilmore@eece.unm.edu).

A. Ware is with the Department of Physics and Astronomy, University of Montana, Missoula, MT 59812 USA.

Color versions of one or more of the figures in this paper are available online at http://ieeexplore.ieee.org.

Digital Object Identifier 10.1109/TPS.2013.2296535

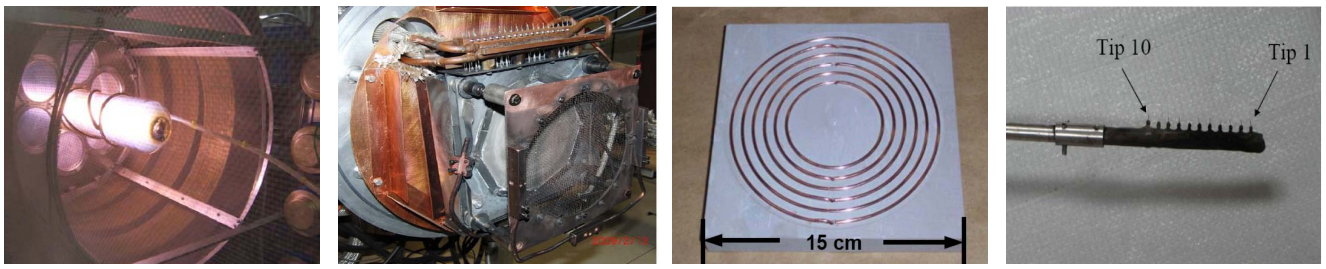

(a) (b) (c) (d)

Fig. 2. (a) Helicon source during operation in helium. Visible is the Pyrex tube and antenna strap. (b) Cathode source. (c) Copper concentric bias rings mounted on ceramic substrate. Ring radii are 3.0, 3.7, 4.4, 5.1, 5.9, and 6.6 cm. (d) Multipoint rake probe.

optimal control problem is solved to determine the control laws for the bias ring voltages that minimize a cost functional related to the amplitude of the fluctuations. Among many optimization techniques that may be considered, extremum seeking [5] has been chosen to address this challenge since this technique can be applied directly to the plant in real time without the need of using any dynamic model. This is critical in this application, where the models are incomplete and where the model predictions may still differ significantly from the experimental observations. After implementing the extremum-seeking controller in HELCAT, the experimental results show both the capability of the bias rings to affect the fluctuation level and the capability of the control algorithm to not only suppress the fluctuations but also regulate their average amplitude around a predefined desired level. Second, the extremum-seeking control approach is also proven effective in regulating the azimuthal flow profile around a prescribed target profile. While under development, a multipoint probe capable of simultaneously measuring the azimuthal flow at different points along the plasma radius, as required by the controller, is currently not available in HELCAT. Therefore, the analysis of this approach is based on predictions by a HELCAT-tailored transport code. Optimal control laws for the strengths of the momentum sources (relationships between bias ring voltages and momentum source strengths are still not modeled in the transport code) are determined by minimizing a cost function related to the error between actual and target azimuthal flow profiles.

This paper is organized as follows. HELCAT is briefly described in Section II. The transport model implemented in the predictive code used for testing of the extremum-seeking algorithms is summarized in Section III. Fundamentals of the extremum seeking algorithm are introduced in Section IV. The implementation of the extremum-seeking controller in HELCAT device to suppress and regulate the plasma fluctuations is presented in Section V together with the analysis of the experimental results. The use of the extremum-seeking controller for direct regulation of the azimuthal flow profile is introduced in Section VI together with numerical results based on the HELCAT predictive transport code. Finally, conclusion and future goals are stated in Section VII.

II. HELCAT Plasma Device

The HELCAT linear plasma device at the University of New Mexico (UNM), shown in Fig. 1, consists of a 4-m long and

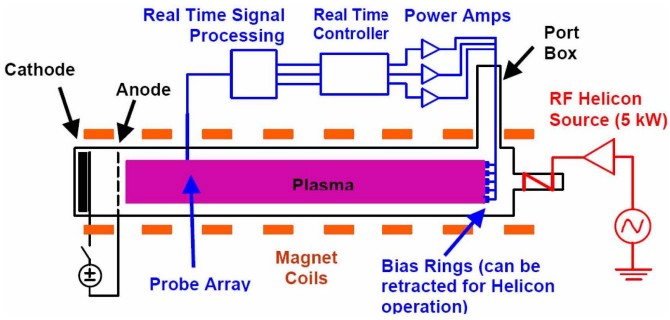

Fig. 3. Schematic view of HELCAT feedback control system.

50-cm diameter cylindrical stainless steel vacuum chamber in two 2-m sections. Each section has eight 10-in, twelve 8-in, and fourteen 3.375-in conflat type ports providing excellent diagnostic access. Currently, four 10-in gate valves and seven KF-40 differentially pumped linear probe feedthroughs provide diagnostic access while under vacuum. Magnetic fields are produced by a total of 13 water-cooled solenoidal magnetic coils (steady-state magnetic fields of up to 2.2 kG at 500 A) [1].

HELCAT is a dual-source plasma device that makes use of two different sources with different ionization mechanisms. These are the helicon source and the thermionic cathode sources located at the two ends of the vacuum chamber [Fig. 2(a) and (b)]. The helicon source is usually characterized by producing high-density plasmas with peaked profiles and relatively long discharge times. On the other hand, the cathode source is capable of producing lower density plasmas with broader profiles and shorter discharge times. Cathode sources also generate hotter plasmas when compared with helicon sources. Although each source can be operated separately, with both sources acting simultaneously, it is possible to operate HELCAT over a wide range of plasma collisionalities (via changes in background neutral pressure).

A typical hardware configuration used for real-time control in HELCAT is shown in Fig. 3. There are six concentric bias rings located at the helicon end of the plasma column. The voltages of the bias rings are used by the control system to manipulate the $E \times B$ flow profiles. The configuration of the bias rings are shown in Fig. 2(c). The rings are located on a ceramic substrate and are separated by gaps of approximately 7 mm. Ring radii are 3.0, 3.7, 4.4, 5.1, 5.9, and 6.6 cm. A set of four 400-W Kepco BOP-20-20M power operational

amplifiers, which can source or sink up to 20 A at 20 V with a 10-kHz/20 V slew rate, is available for fast ring biasing. In addition, several 12 V car batteries can be used to apply dc bias to rings. The real-time controller hardware contains set of rack-mounted compact PCI digitizers (32 channels, 500 Ksamples/s, and 12 bits), with an on-board embedded Linux system. This system is controlled by a host PC running Linux and Labview. For real-time control, the system is operated in low-latency mode, which allows 32 inputs read, control decisions made, and outputs written in 120 μs [2].

III. HELCAT Transport Model

Transport models are used to describe the qualitative response of the plasma profiles to the actuators (concentric bias rings) for a specified scenario. Recent models have included neoclassical and turbulent transport processes as well as the interplay between pressure gradients, flow generation, and radial electric field shear. In this section, the transport model developed in [6] is introduced. This model predicts the radial-temporal evolution of the flux-surface averaged density, $n(r,t)$, electron temperature, $T_e(r,t)$, ion temperature, $T_i(r,t)$, axial velocity, $V_z(r,t,)$, azimuthal velocity, $V_\theta(r,t)$, rms fluctuation amplitude, $\varepsilon(r,t)$, and radial electric field, $E_r(r,t)$, where r and t, respectively, denote the radial and temporal variables.

The evolution of the density is governed by

$$\frac{\partial n}{\partial t} = s + \frac{1}{r}\frac{\partial}{\partial r}\left[r D_n \frac{\partial n}{\partial r}\right] \tag{1}$$

where s is the power deposition profile, which is modeled by a flat-top radial profile

$$s(r) = \begin{cases} S_0, & r \le w_s \\ 0, & r > w_s \end{cases} \tag{2}$$

where w_s is the radial width of the source and S_0 is the cathode/helicon source. The term D_n on the right-hand side (RHS) of (1) is the total particle diffusivity, which includes both neoclassical and turbulent effects. It is modeled by

$$D_n = D_0 + \mu_{\text{prof}} D_{0_b} \sqrt{\frac{T_e}{\left|\frac{1}{T_e}\frac{\partial T_e}{\partial r} + \frac{1}{n}\frac{\partial n}{\partial r}\right|}}\,\varepsilon^2 \tag{3}$$

where D_0 (collisional particle transport coefficient), D_{0_b} (turbulent particle transport coefficient), and μ_{prof} (turbulent transport profile modification) are all constants.

The evolution of the electron temperature, $T_e(r,t)$, and the ion temperature, $T_i(r,t)$, are governed by the following two partial differential equations (PDEs):

$$\begin{aligned}\frac{3n}{2}\frac{\partial T_e}{\partial t} &= s\frac{E_{0e}}{T_{e0}} + \frac{1}{r}\frac{\partial}{\partial r}\left[r\left(D_{T_e} n\frac{\partial T_e}{\partial r} + \frac{5}{2}D_n T_e \frac{\partial n}{\partial r}\right)\right] \\ &\quad + D_n \frac{1}{n}\frac{\partial n}{\partial r}\frac{\partial n T_i}{\partial r} - q_b\sqrt{\frac{1}{T_e}}n^2\left(1 - \frac{T_{i0}T_i}{T_{e0}T_e}\right) \end{aligned} \tag{4}$$

$$\begin{aligned}\frac{3n}{2}\frac{\partial T_i}{\partial t} &= s\frac{E_{0i}}{T_{i0}} + \frac{1}{r}\frac{\partial}{\partial r}\left[r\left(D_{Ti} n\frac{\partial T_i}{\partial r} + \frac{5}{2}D_n T_i \frac{\partial n}{\partial r}\right)\right] \\ &\quad - D_n \frac{1}{n}\frac{\partial n}{\partial r}\frac{\partial n T_i}{\partial r} + q_b\sqrt{\frac{1}{T_e}}n^2\left(\frac{T_{e0}}{T_{i0}} - \frac{T_i}{T_e}\right) - \mu_{cx} n T_i \end{aligned} \tag{5}$$

where the electron and ion power sources (E_{0e} and E_{0i}, respectively), the electron and ion normalization factors (T_{e0} and T_{i0}), the ion–electron energy exchange factor, q_b, and the normalized charge exchange flow damping factor, μ_{cx}, are all constants. The first terms on the RHSs of (4) and (5) represent the cathode electron and ion energy inputs, respectively. The second terms reflect the summation of conductive and convective energy fluxes. The third terms are describing the ion–electron friction, whereas the fourth terms represent the ion–electron energy transport. Finally, the additional last term on the RHS of (5) represents the charge-exchange damping.

The axial velocity equation is

$$\begin{aligned}\frac{\partial V_z}{\partial t} &= \alpha_z \frac{\partial}{\partial r}\left(r^2\,\varepsilon\,\frac{\partial \varepsilon}{\partial r}\frac{\partial E_r}{\partial r}\right) + s V_{z0\text{in}} - \mu V_z \\ &\quad + \frac{1}{r}\frac{\partial}{\partial r}\left(r D_{V_z}\frac{\partial V_z}{\partial r}\right) \end{aligned} \tag{6}$$

where α_z (the axial flow generation parameter), $V_{z0\text{in}}$ (the axial momentum input from the source), and μ (the flow damping multiplier) are all constants and D_{V_z} is the diffusivity of the axial velocity. By definition, $D_{V_z} = D_n$, where D_n is given by (3). The first term on the RHS of (6) is related to the Reynolds stress flow generation, the second term represents the axial momentum source from the helicon, third term represents the charge-exchange flow damping, and the last term is related to the flux divergence of the axial velocity.

The poloidal, or azimuthal, flow equation is

$$\begin{aligned}\frac{\partial V_\theta}{\partial t} &= S_\theta - \mu V_\theta + \frac{1}{r}\frac{\partial}{\partial r}\left[r D_{V_\theta}\frac{\partial V_\theta}{\partial r}\right] \\ &\quad + \alpha_\theta \frac{\partial}{\partial r}\left[r^2 \varepsilon \frac{\partial \varepsilon}{\partial r}\frac{\partial E_r}{\partial r}\right]\left(\frac{2}{r^2 f_{\text{ac}}}\right) \end{aligned} \tag{7}$$

where S_θ is the azimuthal flow (momentum) source, D_{V_θ} is the diffusivity of the azimuthal velocity, α_θ is the azimuthal flow generation parameter, and f_{ac} is the Reynolds stress suppression term. Note that the azimuthal flow diffusivity, D_{V_θ}, is modeled in the same way as the total particle diffusivity, D_n in (3), with D_0 10 times greater, D_{0b} 50 times greater, and the same μ_{prof}. The Reynolds stress suppression term, f_{ac}, is a function of the plasma radius given by

$$f_{\text{ac}}(r) = 1 + 10^{-6}\left[\frac{1}{(1.000001 - r)^6} + \frac{1}{(0.000001 + r)^6}\right]. \tag{8}$$

The evolution equation for the radial electric field is governed by

$$E_r = \alpha_{\text{diag}}.\alpha\left(\frac{\partial T_i}{\partial r} + T_i\frac{1}{n}\frac{\partial n}{\partial r}\right) - V_{\theta_{\text{norm}}} V_\theta \tag{9}$$

where α_{diag} is the factor used to turn off the diamagnetic effects on E_r, α is the normalization factor for the diamagnetic terms, and $V_{\theta_{\text{norm}}}$ is the normalization factor for the azimuthal flow.

Finally, the evolution of the rms fluctuation is governed by

$$\begin{aligned}\frac{\partial \varepsilon}{\partial t} &= \left\{\gamma - \alpha_{\varepsilon_1}\alpha_1 \varepsilon\left|\frac{1}{n}\frac{\partial n}{\partial r}\right|^{-\frac{1}{4}} - \alpha_{\varepsilon_2}\left[r\frac{\partial}{\partial r}\left(\frac{E_r}{r}\right)\right]^2\right\}\varepsilon \\ &\quad + \frac{1}{r}\frac{\partial}{\partial r}\left[r D_\varepsilon \frac{\partial \varepsilon}{\partial r}\right] \end{aligned} \tag{10}$$

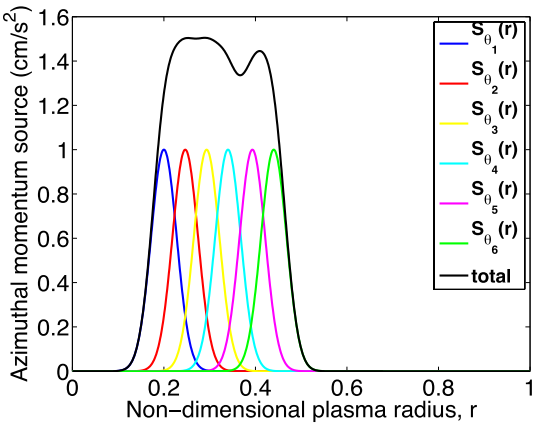

Fig. 4. Gaussian momentum sources.

where $\varepsilon \equiv \sqrt{<(\tilde{n}/n)^2>}$ ($\tilde{n}$ is the density fluctuation), D_ε is the diffusivity of the turbulence, which equals the total particle diffusivity given in (3), and γ is the growth rate factor given by

$$\gamma = g\gamma_0 \nu_{\rm ei} T_e \left(\frac{1}{n}\frac{\partial n}{\partial r}\right)^2 \tag{11}$$

where g is the time normalization factor, γ_0 is the growth rate multiplier, and $\nu_{\rm ei}$ is the electron–ion collision rate. The growth rate factor in (11) is defined based on the theory of drift wave instabilities in helicon plasmas [7]. The turbulent saturation factor, α_{ε_1}, normalization factor, α_1, and the shear suppression factor, α_{ε_2}, are all constants. The first term on the RHS of (10) represents the fluctuation drive (growth rate), the second term is related to the nonlinear energy transfer (saturation), the third term is the $E \times B$ shear suppression, and the last term represents the diffusion of fluctuations.

The actual control inputs for the HELCAT experiments are the voltages of the biased concentric rings. Their effect can be reproduced using localized Gaussian momentum sources in the predictive transport code. The azimuthal flow source term is then governed by the following model:

$$S_\theta(r) = \sum_{j=1}^{6} p_c(j) \exp\left\{\frac{-[r_p(j)-r]^2}{2[w_{\rm pc}(j)]^2}\right\} \tag{12}$$

where p_c (momentum source strengths), r_p (radial positions of the momentum source), and $w_{\rm pc}$ (momentum source widths) are all 6-D arrays that describe the characteristics of the Gaussian momentum source.

The actual bias ring positions of the HELCAT device are 0.2, 0.24666667, 0.29333333, 0.34, 0.39333333, and 0.44 in normalized radius with respect to the plasma radius. For $p_c(j) = 1$ and $w_{pc}(j) = 0.028\ \forall j = 1, \ldots, 6$, the azimuthal momentum source is shown in Fig. 4. The black curve represents the total azimuthal flow source, $S_\theta(r)$, while the individual contributions of the bias rings are shown by the separate curves plotted in color.

The predictive code based on the model (1)–(12) is still under development and validation but it already provides qualitative predictions that match experimental observations.

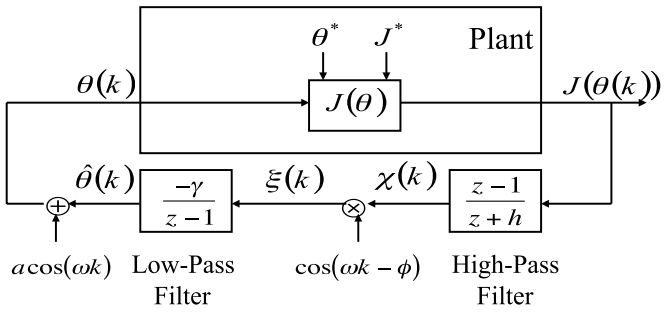

Fig. 5. Extremum seeking control scheme for discrete-time systems.

However, there are two key differences at this moment between the numerical code and the experiment:

1) although the numerical code can predict the evolution of the rms envelope of the fluctuation ε based on (10), in the real experiment, we can only measure a signal that is proportional to the fluctuation as it will be explained in the following;
2) while in the numerical code, the control inputs are the strengths $p_c(j)$ of the momentum sources, as defined in (12), in the real experiment, the control inputs are the voltages of the bias rings. These voltages create an electrical field in the radial direction that by interacting with the axial magnetic field produces torque in the poloidal or azimuthal direction.

IV. Extremum Seeking Optimal Control

Extremum seeking can be applied in nonlinear problems if the nonlinearity has a local minimum or maximum. The origin of the nonlinearity may be due to the plant itself or due to the control objective imposed on the plant in the form of a cost functional of an associated optimization problem. Therefore, extremum seeking is applicable either for finding the set point that corresponds to the optimal output, or for tuning the parameters of a feedback control law [5]. The former application is used in this paper to achieve either a desired level of rms fluctuation (Section V) or a target azimuthal velocity profile (Section VI) in the HELCAT device.

In the experimental studies (Section V), the to-be-optimized vector parameter θ represents the voltages of the concentric bias rings, whereas in numerical studies (Section VI), the to-be-optimized vector parameter θ represents the azimuthal momentum source strengths, $p_c(j)$, in (12). The value of the vector θ is changed systematically after each plasma discharge. In a simulation environment, the term discharge refers to the integration of the PDEs described in Section III. Since the variable θ is changed or tuned after each plasma discharge, it is convenient to apply the discrete time version of the extremum seeking algorithm [5], [8]. The implementation of the extremum seeking control scheme is shown in Fig. 5, where z stands for the Z-transform variable. The static nonlinear block $J(\theta)$ in Fig. 5 represents the to-be-optimized cost function. The variable θ^* represents the minimizing values of θ, whereas J^* represents the corresponding minimum value of the cost function, J. Therefore, $J^* = J(\theta^*)$.

The objective of the extremum seeking algorithm is then to drive $\theta - \theta^*$ to zero to drive $J(\theta)$ to its optimal

value, J^* [5]. The variable $\hat{\theta}$ in Fig. 5 represents the estimation of the unknown optimal input θ^*. The probing signal $a\cos(\omega k)$, which is added to the estimate $\hat{\theta}$ and then fed into the plant, yields a measure of the gradient information of the map $J(\theta)$. The role of the high-pass filter is to extract only the perturbation in the cost functional J caused by the perturbation in the θ parameter created by the probing signal. The effect of the demodulation, $\cos(\omega k - \phi)$, is to reveal only the component of the filtered perturbed cost functional χ having the same frequency ω as the probing signal. Finally, the signal ξ is fed into the pure-integrator low-pass filter to update the θ parameter to drive the cost functional J to its minimum [8]. The discrete-time extremum seeking algorithm shown in Fig. 5 can be summarized as follows:

$$\chi(k) = -h\chi(k-1) + J(k) - J(k-1) \tag{13}$$

$$\xi(k) = \chi(k)\cos(\omega k - \phi) \tag{14}$$

$$\hat{\theta}(k+1) = \hat{\theta}(k) - \gamma\xi(k) \tag{15}$$

$$\theta(k+1) = \hat{\theta}(k+1) + a\cos(\omega(k+1)). \tag{16}$$

The high-pass filter, $z - 1/(z+h)$, is designed as $0 < h < 1$, and the modulation frequency ω is selected such that $\omega = \alpha\pi$, $0 < |\alpha| < 1$, where α is rational. It is important to select ω large in a qualitative sense when compared with the plant time scale. The cutoff frequencies of the filters need to be lower than the frequency ω of the probe signal. These observations impose constraints and, at the same time, a relationship between ω and h. As an additional constraint, ω should not equal any frequency present in the measurement noise. The perturbation amplitude a needs to be small to make the steady-state output error also small. Given a, the adaptation gain γ of the low-pass filter needs to be small enough to preserve stability [5], [8].

In this case, we are dealing with a multiparameter extremum seeking procedure. Note that, as described in Section II, only four power supplies are available in the actual HELCAT machine. Hence, only four out of the six bias rings can be controlled independently. Therefore, the extremum seeking variables are defined to have four components given by

$$\theta(k) = \begin{bmatrix}\theta_1(k)\\ \theta_2(k)\\ \theta_3(k)\\ \theta_4(k)\end{bmatrix}, \quad \hat{\theta}(k) = \begin{bmatrix}\hat{\theta}_1(k)\\ \hat{\theta}_2(k)\\ \hat{\theta}_3(k)\\ \hat{\theta}_4(k)\end{bmatrix}, \quad \xi(k) = \begin{bmatrix}\xi_1(k)\\ \xi_2(k)\\ \xi_3(k)\\ \xi_4(k)\end{bmatrix}.$$

Similarly, the perturbation terms are

$$\cos(\omega k) = \begin{bmatrix}\cos(\omega_1 k)\\ \cos(\omega_2 k)\\ \cos(\omega_3 k)\\ \cos(\omega_4 k)\end{bmatrix}, \quad \cos(\omega k + \phi) = \begin{bmatrix}\cos(\omega_1 k + \phi_1)\\ \cos(\omega_2 k + \phi_2)\\ \cos(\omega_3 k + \phi_3)\\ \cos(\omega_4 k + \phi_4)\end{bmatrix}.$$

The extremum seeking constants in Fig. 5 are diagonal matrices given by

$$a = \begin{bmatrix}a_1 & 0 & 0 & 0\\ 0 & a_2 & 0 & 0\\ 0 & 0 & a_3 & 0\\ 0 & 0 & 0 & a_4\end{bmatrix}, \quad \gamma = \begin{bmatrix}\gamma_1 & 0 & 0 & 0\\ 0 & \gamma_2 & 0 & 0\\ 0 & 0 & \gamma_3 & 0\\ 0 & 0 & 0 & \gamma_4\end{bmatrix}.$$

V. Fluctuation Mitigation and Regulation

In this section, the potential of an extremum-seeking optimal controller for regulating the fluctuation level by adaptively tuning the bias ring voltages is illustrated experimentally in HELCAT. The optimal control laws for the bias ring voltages are determined using the extremum seeking algorithm (13)–(16) to minimize a cost function related to the rms fluctuation amplitude.

A. Experimental Setup

Due to the availability of only four power supplies, the three outer bias rings shown in Fig. 2(c) have been connected in parallel. Therefore, while the voltages of the three inner rings can be controlled independently, the voltages of the three outer rings can be controlled only as a group. The power suppliers are grounded to the HELCAT chamber and their output ranges are −20 V/+20 V. With the experimental observations obtained in a trial and error procedure, the power supplies for the two inner rings have been connected in series with 12 V car batteries to improve the efficiency of the bias rings in terms of fluctuation mitigation. The ranges for the two inner power supplies are −8 V/+32 V. Tips 3, 5, 6, and 8 of the rake probe shown in Fig. 2(d) have been used to simultaneously obtain fluctuation-related measurements at several points along the plasma radius.

B. Extremum Seeking Setup

For this application, the cost function of the extremum seeking algorithm is defined as

$$J = \sum_{i=1}^{4} k_i J_i \tag{17}$$

where k_i are weighting constants and J_i are functions of the rms fluctuation ε at different points in space r_i $(i = 1, \ldots, 4)$ averaged over a predefined period of time

$$J_i = J_i(\bar{\varepsilon}(r_i, \theta)) \triangleq \bar{\varepsilon}(r_i, \theta), \tag{18}$$

where

$$\bar{\varepsilon}(r_i, \theta) = \frac{1}{t_2 - t_1}\int_{t_1}^{t_2} \varepsilon(t, r_i, \theta)dt \tag{19}$$

with $t_1 = 100$ ms and $t_2 = 250$ ms in (19). This choice of the time interval is based on the fact that the transient dampens out after 80 ms and the plasma is considered to be in quasi steady state for $100 \leq t \leq 250$ ms. We define $\theta_1 = V_1$, $\theta_2 = V_2$, $\theta_3 = V_3$, and $\theta_4 = V_4$, where V_i, for $i = 1, \ldots, 4$, represent the voltages on the bias rings R_1, R_2, R_3, and $R_4/R_5/R_6$, respectively (R_1 denotes the most inner ring while R_6 denotes the most outer ring). The radii r_i, for $i = 1, \ldots, 4$, denote the positions of the tips 3, 5, 6, and 8 of the rake probe shown in Fig. 2(d). In each iteration k of the extremum seeking procedure, or equivalently, in each plasma run, we fix $\theta(k)$ (bias ring voltages V_i) and obtain direct or indirect time-averaged measurements of the rms fluctuation at four points in space, i.e., $\bar{\varepsilon}(r_i, \theta(k)))$ for $i = 1, \ldots, 4$. These measurements are used to compute $J(\theta(k))$, as defined in (17) and (18),

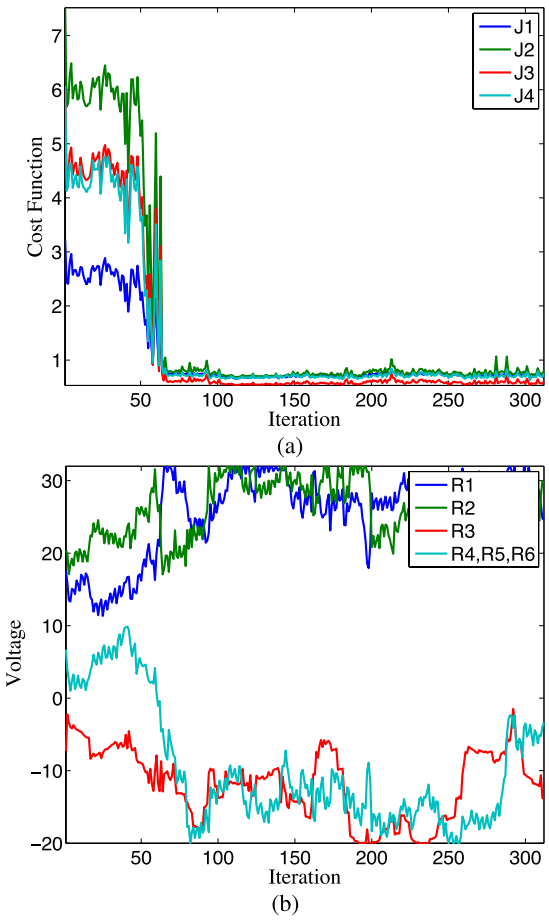

Fig. 6. (a) Experimental cost function components. (b) Ring voltages (θ).

which is in turn fed into the extremum-seeking algorithm (13)–(16) to compute $\theta(k+1)$. The extremum seeking parameters are tuned as $h = 0.4$, $\omega_i = 0.065i\pi$, for $i = 1, \ldots, 4$, and $\gamma = 0.5$ based on the numerical predictions provided by the predictive transport code (1)–(12).

C. Experiment Results

The experimental results obtained after the implementation in HELCAT of the extremum seeking algorithm (13)–(16) with cost function (17) and (18) are presented in the following.

1) Fluctuation Mitigation: The first extremum-seeking implementation in HELCAT focused on fluctuation mitigation. The goal in this case is to reduce the fluctuation level and completely suppress it if possible. Although the numerical code can predict the evolution of the rms fluctuation ε based on (10), it is not easy to directly measure this quantity in the real HELCAT device. Hence, for the experiments, the cost function (17) and (18) are defined in terms of the ion saturation current, which can be related to the fluctuation as it will be explained in the following. With this modification, the cost function of the experimental procedure becomes

$$J_i(\bar{\varepsilon}(r_i,\theta)) = \bar{I}_s\,(r_i,\theta)\,, \tag{20}$$

where

$$\bar{I}_s(r_i,\theta) = \frac{1}{t_2-t_1}\int_{t_1}^{t_2}\sqrt{\tilde{I}_s^2(t,r_i,\theta)}dt \tag{21}$$

$$\tilde{I}_s(t,r_i,\theta) = I_s(t,r_i,\theta) - I_s^o(r_i,\theta) \tag{22}$$

$$I_s^o(r_i,\theta) = \frac{1}{t_2-t_1}\int_{t_1}^{t_2} I_s(t,r_i,\theta)dt \tag{23}$$

with $t_1 = 100$ ms and $t_2 = 250$ ms. I_s denotes the ion saturation current signal provided by the rake probe, which is proportional to $\sqrt{T_e}n$. If we write $T_e \approx <T_e> + \tilde{T}_e$ and $n \approx <n> + \tilde{n}$, where $<>$ denotes average or zeroth order contribution and $\sim$ denotes fluctuation or first order contribution, and consider that the T_e fluctuation is very small compared with its average value, we can conclude that $I_s \propto \sqrt{<T_e>} < n > + \sqrt{<T_e>}\tilde{n}$. This implies that $\tilde{I}_s \propto \tilde{n}$, and therefore $\bar{I}_s$ is an indirect measure of $\bar{\varepsilon}$.

Fig. 6(a) shows the evolutions of the four components $J_i(\bar{\varepsilon}(r_i,\theta)) = \bar{I}_s\,(r_i,\theta)$ of the cost function, where r_i, for $i = 1, \ldots, 4$, represent the positions of tips 3, 5, 6, and 8 of the rake probe, as a function of the extremum seeking iterations, i.e., as a function of the HELCAT plasma discharges. We can note that after 60 discharges, the fluctuation is driven to a much lower level than that presents before turning on the extremum seeking controller. The evolutions of the components of the extremum-seeking θ parameter, which are the voltages provided by the four power amplifiers, are shown in Fig. 6(b). We can observe that the two inner bias ring voltages are driven by the extremum seeking algorithm to positive values around 25 V, while the voltages of the four outer bias rings are driven to negative values around -10 V. Fig. 7 shows time evolution of the ion saturation current, whose variance is proportional to the density fluctuation, before and after turning on the extremum-seeking controller at the four spatial locations defined by the positions of tips 3, 5, 6, and 8 of the rake probe. By comparing Fig. 7(a)–(d), it is possible to note that the fluctuation phenomenon is indeed more severe at the far edge of the plasma. After the extremum-seeking controller is turned on, Fig. 7 shows that the fluctuation levels measured by the four tips of the probe are dramatically reduced. By comparing Fig. 7(e)–(h), we can note that extremum seeking is effective in mitigating fluctuation both at the center and at the edge of the plasma.

2) Fluctuation Regulation: The second extremum-seeking implementation focused on fluctuation regulation. The goal in this case is not to suppress fluctuation but to regulate it around a desired level. Therefore, the cost function (17) and (18) are redefined for this application as follows:

$$J_i(\bar{\varepsilon}(r_i,\theta)) = \sqrt{\left(\bar{I}_s\,(r_i,\theta) - \bar{I}_s^*\,(r_i)\right)^2}, \tag{24}$$

where $\bar{I}_s^*$ denotes the desired value of $\bar{I}_s\,(r_i,\theta)$, which is related to a desire value for $\bar{\varepsilon}$. We set $\bar{I}_s^*(r_1) = 2$, $\bar{I}_s^*(r_2) = 4$, $\bar{I}_s^*(r_3) = 3$, and $\bar{I}_s^*(r_4) = 3$.

Fig. 8(a) shows the evolutions of $\bar{I}_{si} = \bar{I}_s(r_i)$, where r_i, for $i = 1, \ldots, 4$, represent the positions of tips 3, 5, 6, and 8 of the rake probe, as a function of the extremum seeking iterations, or equivalently, the HELCAT plasma discharges. Note that the extremum seeking controller drives

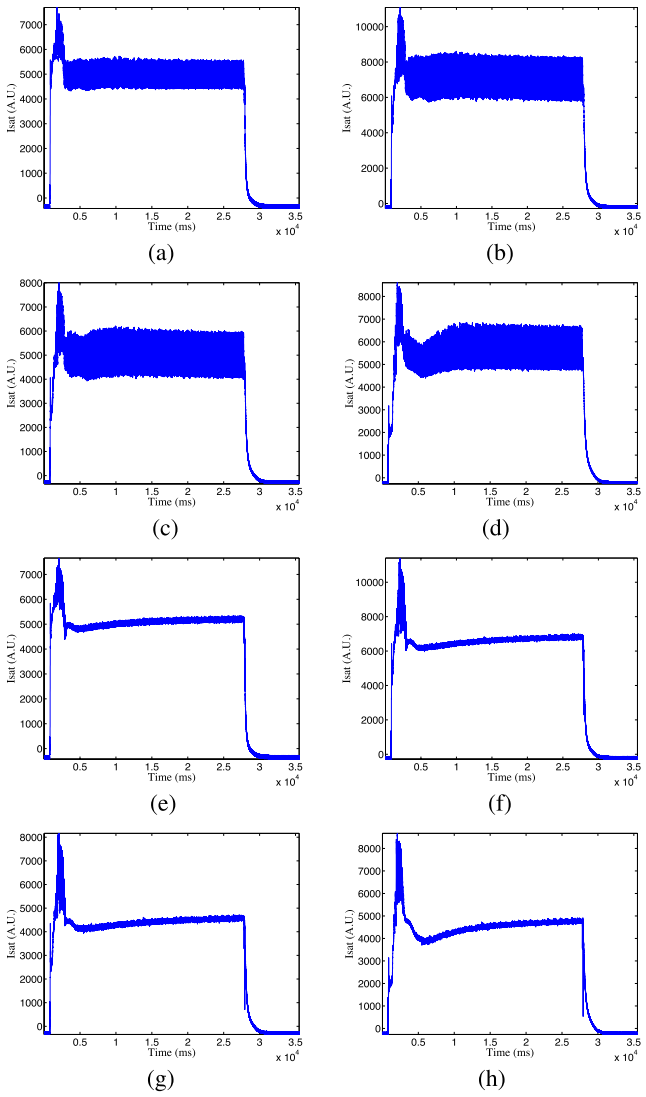

Fig. 7. Ion saturation current evolution before the extremum seeking controller is turned on (a) tip 3, (b) tip 5, (c) tip 6, and (d) tip 8, and after the extremum seeking controller is turned on (e) tip 3, (f) tip 5, (g) tip 6, and (h) tip 8.

$\bar{I}_s(r_1) \rightarrow \sim 2$, $\bar{I}_s(r_2) \rightarrow 5$, $\bar{I}_s(r_3) \rightarrow 3.5$, and $\bar{I}_s(r_4) \rightarrow 3.5$. It is important to emphasize that the desired values $\bar{I}^*_{si}$, for $i = 1, \ldots, 4$, have been chosen arbitrarily and there is no guarantee that they are indeed achievable.

The evolutions of the components of the extremum-seeking parameter θ, which are the voltages provided by the four power amplifiers, are shown in Fig. 8(b). Fig. 9 shows the time evolution of the ion saturation current, whose variance is proportional to the density fluctuation, before and after turning on the extremum-seeking controller at the four spatial locations defined by the positions of the tips of the rake probe. After the extremum-seeking controller is turned on, Fig. 9 shows that the fluctuation levels measured by the four tips of the probe are reduced but not suppressed. It is interesting to note the sudden change in the fluctuation level at around 150 ms. This phenomenon may be related to the fact that the to-be-minimized cost function is defined in terms of the time average of the fluctuation. The extremum seeking controller

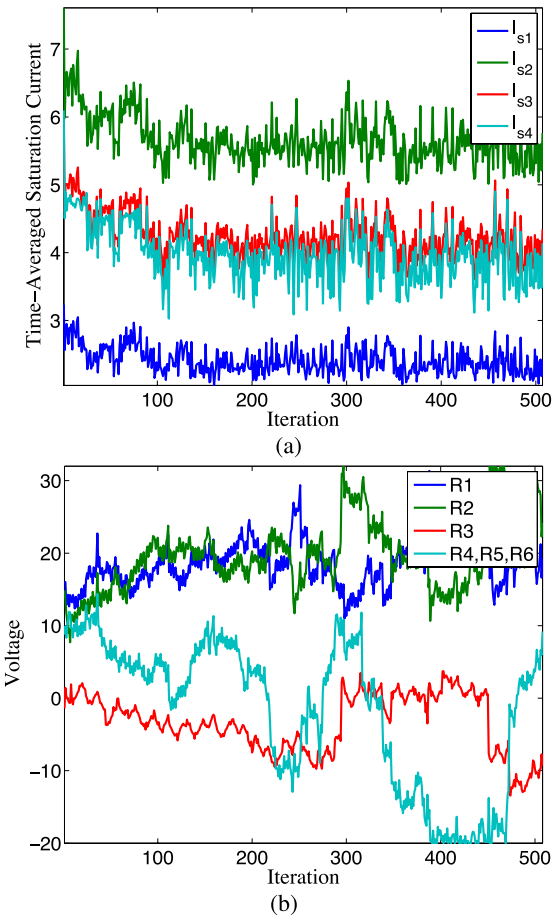

Fig. 8. (a) Experimental time-averaged ion saturation current components. (b) Ring voltages (θ).

seems to drive the voltages to values where this sudden change is possible to achieve the time-averaged level of fluctuation specified by I^*_{si}, for $i = 1, \ldots, 4$. By comparing Fig. 9(e)–(h), one can note that extremum seeking is effective in mitigating fluctuation both at the center and at the edge of the plasma.

VI. Azimuthal Velocity Profile Regulation

The radial derivative of the azimuthal flow (i.e., the flow shear) has been shown effective in increasing or decreasing the drift wave turbulence at the plasma edge [4]. Hence, the turbulent fluctuations could be controlled indirectly in HELCAT by controlling the azimuthal flow profile evolution, $V_\theta(r, t)$. Once the radial azimuthal velocity profile associated with a particular level of rms fluctuation is identified, the challenge of systematically achieving and sustaining such profile still remains. An extremum-seeking optimal controller can also be useful to regulate the azimuthal flow profile around a prescribed target profile, as is illustrated in this section. Real-time measurements of the azimuthal flow velocity must be available at several radial points within the plasma to achieve this goal. While under development, a multipoint probe capable of simultaneously measuring the azimuthal flow at different points along the plasma radius is currently not available in HELCAT. Therefore, the results presented in this section are limited to the numerical simulations based on the

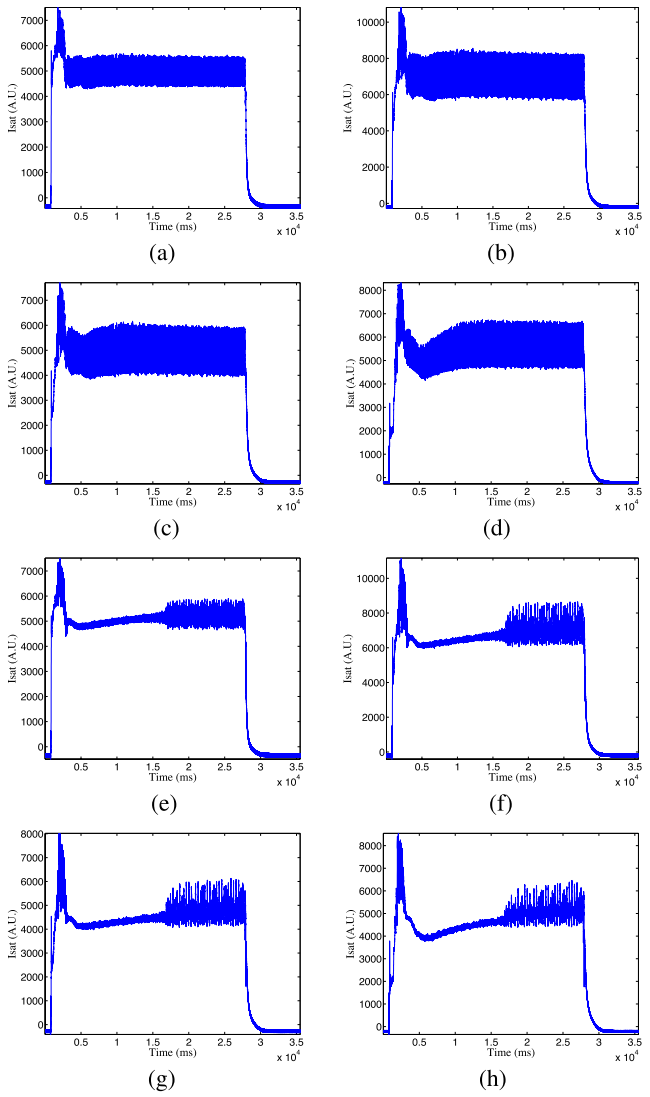

Fig. 9. Ion saturation current evolution before the extremum seeking controller is turned on (a) tip 3, (b) tip 5, (c) tip 6, and (d) tip 8, and after the extremum seeking controller is turned on (e) tip 3, (f) tip 5, (g) tip 6, and (h) tip 8.

transport code introduced in Section III. The optimal control laws for the strengths of the momentum sources (as discussed in Section III, the relationships between bias ring voltages and momentum source strengths are still not modeled in the transport code) are determined using the extremum seeking algorithm (13)–(16) with a cost function that represents the error between actual and target azimuthal flow profiles.

A. Numerical Setup

In the actual HELCAT device, only four out of the six bias rings can be controlled independently. Hence, the extremum seeking algorithm is designed to regulate only four source strengths while the two additional source strengths are fixed.

B. Extremum Seeking Setup

For this application, we define the cost function as

$$J = \sqrt{\int_0^{r_a} [V_\theta(r,T) - V_\theta{}^*(r)]^2\, dr} \tag{25}$$

where $V_\theta{}^*(r)$ is the target azimuthal velocity profile at $T = 250$ ms and $r_a = 15$ cm is the plasma radius. In each iteration k of the extremum seeking procedure, we fix $\theta(k)$ and obtain direct or indirect measurements of the azimuthal velocity profile at N points along the plasma radius, i.e., $V_\theta(r_i, T)$ for $i = 1, \ldots, N$. The definite integral in (25) can be discretized approximately as follows:

$$J(k) = J(\theta(k)) \approx \sqrt{\sum_{i=1}^{N} [V_\theta(r_i,T) - V_\theta{}^*(r_i)]^2}. \tag{26}$$

Equation (26) is then fed into the extremum-seeking algorithm, (13)–(16) to compute $\theta(k+1)$.

C. Numerical Results

The effectiveness of the proposed extremum seeking controller is tested through the numerical simulations using the predictive transport code for HELCAT introduced in Section III. For this purpose, the extremum seeking algorithm (13)–(16) with cost function (26) is coupled with the transport model (1)–(12).

A first extremum-seeking simulation study is performed by generating the target azimuthal velocity profile using the following arbitrary values for the azimuthal momentum source strengths (p_c):

$$p_c = [-10 \;\; 15 \;\; -20 \;\; 5 \;\; 5 \;\; 5]^T. \tag{27}$$

In this case, the fifth and sixth input channels are fixed at the values associated with the target profile given in (27) while the inner four channels are regulated by the extremum seeking controller, i.e., we define

$$\theta^* = [\theta_1 \;\; \theta_2 \;\; \theta_3 \;\; \theta_4]^T = [p_{c1} \;\; p_{c2} \;\; p_{c3} \;\; p_{c4}]^T. \tag{28}$$

With adequate tuning of the parameters, extremum seeking algorithm generates the actuator wave forms to drive the azimuthal velocity profile to the selected target profile. Fig. 10(a) shows the target V_θ profile together with the profile achieved by the extremum seeking controller at the end of the simulated discharge (250-ms simulation) after 100 iterations. The azimuthal velocity profile V_θ is in normalized (i.e., nondimensional) form. Fig. 10(b) shows the evolution of the cost functional, $J(\theta(k))$, as a function of the extremum seeking iterations. It is observed from Fig. 10(a) and (b) that extremum seeking controller tracks the target profile after 100 iterations as the cost functional becomes almost zero (note from Fig. 10(b) that the tracking is already acceptable after just 60 iterations). Fig. 10(c)–(f) shows the evolutions of the extremum seeking parameters, θ_i, for $i = 1, \ldots, 4$, which are the first four channels of the azimuthal momentum source strengths. It can be noted from these figures that the source strengths estimated by the extremum seeking controller indeed converge to the values associated with the target profile in (27).

A second extremum seeking simulation study is performed by generating the target azimuthal velocity profile using the following values for the azimuthal momentum source strengths (p_c):

$$p_c = [10 \;\; -2 \;\; 10 \;\; -10 \;\; 0 \;\; 5]^T. \tag{29}$$

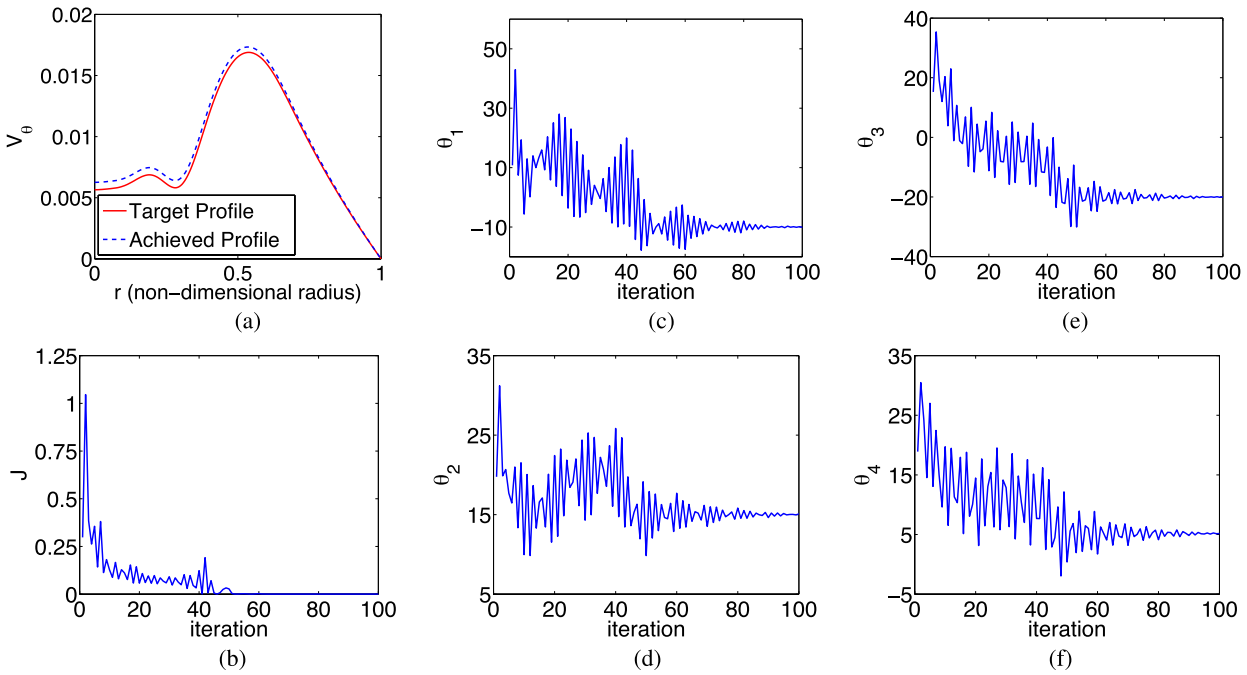

Fig. 10. (a) Target V_θ flow profile and the profile achieved by the extremum-seeking controller (at $t = 250$ ms, for iteration 100). (b) Evolution of the cost function, $J(k)$. (c)–(f) Evolutions of the extremum seeking variables: $\theta_1 = p_c(1)$, $\theta_2 = p_c(2)$, $\theta_3 = p_c(3)$, and $\theta_4 = p_c(4)$.

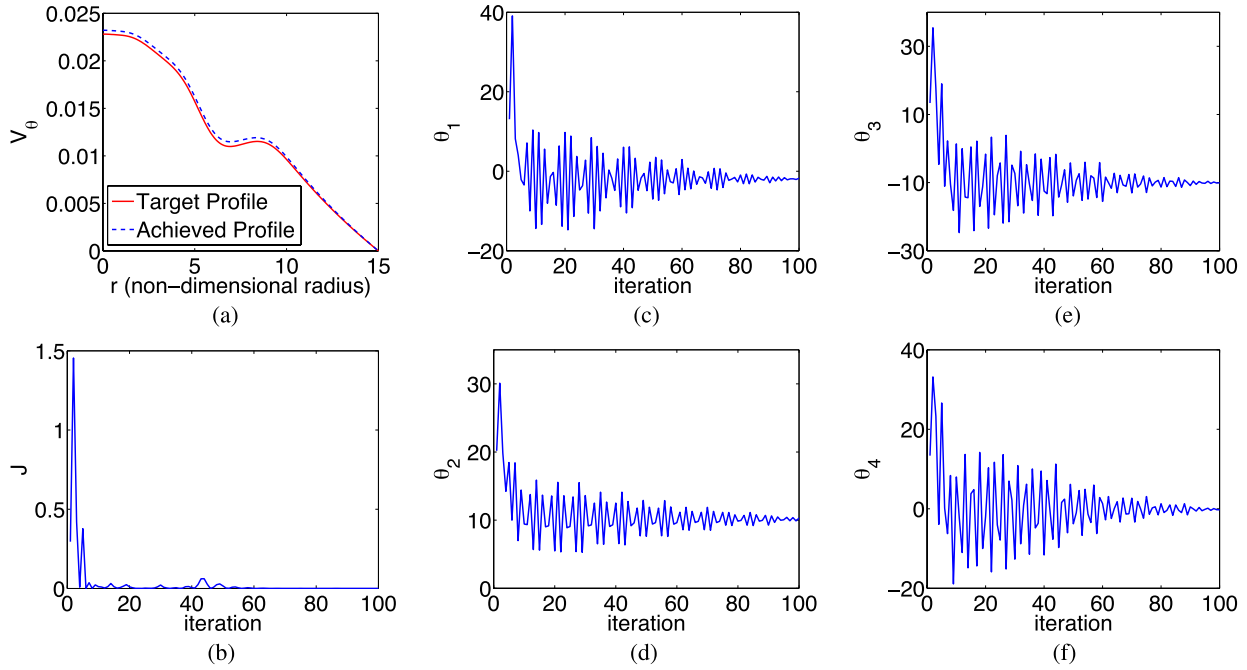

Fig. 11. (a) Target V_θ flow profile and the profile achieved by the extremum-seeking controller (at $t = 250$ ms, for iteration 100). (b) Evolution of the cost function, $J(k)$. (c)–(f) Evolutions of the extremum seeking variables: $\theta_1 = p_c(2)$, $\theta_2 = p_c(3)$, $\theta_3 = p_c(4)$, and $\theta_4 = p_c(5)$.

In this case, the first and last input channels are fixed while the inner four channels are regulated by the extremum seeking controller, i.e., we define

$$\theta^* = [\theta_1 \;\; \theta_2 \;\; \theta_3 \;\; \theta_4]^T = [p_{c2} \;\; p_{c3} \;\; p_{c4} \;\; p_{c5}]^T. \qquad (30)$$

The extremum seeking algorithm is retuned for this case and then the simulations are carried out for 100 iterations. Fig. 11(b) shows the evolution of the cost functional as a function of the extremum seeking iterations. It is observed from Fig. 11(a) that the extremum seeking controller is still effective in matching the target profile at the end of 100 iterations (note from Fig. 11(b) that the matching is already acceptable after just 60 iterations). Fig. 11(c)–(f) shows the actuator waveforms, which show that the source strengths estimated by the extremum seeking controller converge to the values used for the generation of the target profile and given in (29).

VII. Conclusion

Multiparameter extremum-seeking optimal controllers have been designed for both plasma fluctuation mitigation and azimuthal flow profile regulation in HELCAT. The experimental results show that the fluctuation-mitigation controller can fully suppress or successfully regulate the fluctuation level by adaptively tuning the bias ring voltages. This capability of the extremum-seeking controller makes it an extremely useful tool for the study of the underlying physics of the system. The controller's nonmodel-based nature represents an advantage in this case when compared with other model-based optimization techniques due to the challenges arising in the modeling of the system dynamics. The numerical results based on a HELCAT-tailored transport code show that the azimuthal-flow-profile controller is effective in shaping the azimuthal flow profile by adaptively tuning the momentum source strengths. The goal is to implement this controller in the actual HELCAT device as soon as the capability of measuring in real time the azimuthal flow at different radial locations becomes available. The nonmodel-based nature of the extremum-seeking controller will be a clear advantage when transitioning from simulation to experiment. When implemented in HELCAT, the extremum-seeking controller will regulate not the momentum strengths but the ring voltages. Moreover, the controller will consider constraints on the control inputs (voltage rings), which were neglected in the simulation study in this paper.

A multipoint probe capable of simultaneously measuring the poloidal flow at different points along the plasma radius is currently under development. Beyond enabling real-time azimuthal flow profile reconstruction and feedback control, as discussed above, this probe will allow for the identification of the radial azimuthal flow profiles associated with specific levels of fluctuations regulated by the extremum-seeking controller. This application is a clear example on how advanced control techniques can be used as tools to elucidate the physics of laboratory and fusion plasmas.

References

[1] A. G. Lynn, M. Gilmore, C. Watts, J. Herrea, R. Kelly, S. Will, *et al.*, "The HelCat dual-source plasma device," *Rev. Sci. Instrum.*, vol. 80, p. 103501, 2009.

[2] Q. Wang, E. Schuster, M. Gilmore, S. Xie, and A. Ware, "Extremum-seeking-based fluctuation mitigation by E×B actuation in HELCAT," in *Proc. 5th IEEE Multi Conf. Syst. Control*, Sep. 2011, pp. 301–306.

[3] P. W. Terry, "Suppression of turbulence and transport by sheared flow," *Rev. Modern Phys.*, vol. 72, no. 1, pp. 109–165, 2000.

[4] N. Crocker, G. Y. Burin, M. J. Burin, G. R. Tynan, B. P. Cluggish, and K. R. Umstadter, "Control of velocity shear and turbulence through biasing in CSDX," in *Proc. 44th Annu. Meeting APS Division Plasma Phys.*, vol. 47. 2002, p. 264.

[5] K. Ariyur and M. Krstic, *Real-Time Optimization by Extremum Seeking Feedback*. New York, NY, USA: Wiley, 2005.

[6] D. E. Newman, B. A. Carreras, D. Lopez-Bruna, P. H. Diamond, and V. B. Lebedev, "Dynamics and control of internal transport barriers in reversed shear discharges," *Phys. Plasmas*, vol. 5, no. 4, pp. 938–952, 1998.

[7] R. F. Ellis, E. Marden-Marshall, and R. Majeski, "Collisional drift instability of a weakly ionized argon plasma," *Plasma Phys.*, vol. 22, no. 2, pp. 113–132, 1980.

[8] K. A. J. Choi, M. Kristic, and J. Lee, "Extremum seeking control for discrete-time systems," *IEEE Trans. Autom. Control*, vol. 47, no. 2, pp. 318–323, Feb. 2002.

Zeki Okan Ilhan received the B.Sc. degree in mechanical engineering from Middle East Technical University, Ankara, Turkey, in 2010. He is currently pursuing the Ph.D. degree with the Mechanical Engineering and Mechanics Department, Lehigh University, Bethlehem, PA, USA.

He is a member of the Lehigh University Plasma Control Group within the Laboratory for Control of Complex Physical Systems.

Qiaoqiao Wang received the B.Sc. degree in information science and engineering from Northeastern University, Shenyang, China, in 2009, and the M.Eng. degree from the Department of Mechanical Engineering and Mechanics, Lehigh University, Bethlehem, PA, USA, in 2011.

She is a Former Member of the Lehigh University Plasma Control Group within the Laboratory for Control of Complex Physical Systems.

Jason Barry received the B.Sc. degree from the Department of Mechanical Engineering and Mechanics, Lehigh University, Bethlehem, PA, USA, in 2013.

He was involved in research within the Lehigh University Plasma Control Group supported by the National Science Foundation Research Experience for Undergraduates Program.

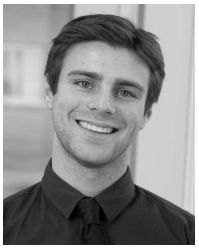

David Huxley-Cohen received the B.Sc. degree in mechanical engineering and environmental sustainability from Lehigh's honors Integrated Degree of Engineering and Arts and Science Program, Lehigh University, Bethlehem, PA, USA, in 2013.

He was with the Lehigh University Plasma Control Group supported by the National Science Foundation Research Experience for Undergraduates Program. He is currently a Presidential Scholar with the Energy Systems Engineering Program, Lehigh University.

Hexiang Wang received the B.Sc. degree in mechanical engineering from the East China University of Science and Technology, Xuhui, China, in 2009, and the M.Sc. degree in mechanical engineering from the University of Manchester, Manchester, U.K., in 2011. He is currently pursuing the M.Sc. degree with the Mechanical Engineering and Mechanics Department, Lehigh University, Bethlehem, PA, USA.

He is a member of the Lehigh University Plasma Control Group, Laboratory for Control of Complex Physical Systems.

Eugenio Schuster received the Undergraduate degrees in electronic engineering from Buenos Aires University, Buenos Aires, Argentina, in 1993, and in nuclear engineering from the Balseiro Institute, Río Negro, Argentina, in 1998, and the M.Sc. and Ph.D. degrees in mechanical and aerospace engineering from the University of California San Diego, San Diego, CA, USA, in 2000 and 2004, respectively.

He is an Associate Professor with the Department of Mechanical Engineering and Mechanics, Lehigh University, Bethlehem, PA, USA. He is the Director of the Laboratory for Control of Complex Physical Systems and the Head of the Lehigh University Plasma Control Group. He was involved in plasma control problems, including equilibrium control, burn control, magnetic and kinetic profile control, and MHD stabilization. His current research interests include distributed-parameter and nonlinear control of nuclear-fusion plasmas.

Prof. Schuster is a recipient of the National Science Foundation Career Award.

Shuangwei Xie, photograph and biography not available at the time of publication.

Mark Gilmore received the B.Sc. degree from Boston University, Boston, MA, USA, the M.Sc. degree from Northeastern University, Boston, and the Ph.D. degree from the University of California, Los Angeles, CA, USA, in 1999, all in electrical engineering.

He is an Associate Professor with the Department of Electrical and Computer Engineering, University of New Mexico, Albuquerque, NM, USA. He was involved in a wide variety of areas within plasma science, including basic physics of turbulence and transport in both laboratory and magnetic fusion plasmas.

Prof. Gilmore serves as the Senior Editor for diagnostics for the IEEE TRANSACTIONS ON PLASMA SCIENCE. He has served on the Plasma Science and Applications Executive Committee of the IEEE Nuclear and Plasma Sciences Society, and the Executive Committee of the University Fusion Association.

Andrew Ware received the B.S. degree from the University of Texas, Austin, TX, USA, in 1988, and the Ph.D. degree from the University of California at San Diego, San Diego, CA, USA, in 1992, both in physics.

He is a Professor with the Department of Physics and Astronomy, University of Montana, Missoula, MT, USA. His current research interests include plasma turbulence, turbulent transport, and 3-D plasma equilibrium, stability, and transport.